Nanoscale

PAPER

View Article Online
View Journal | View Issue

Check for updates

Cite this: *Nanoscale*, 2022, **14**, 15701

Non-equilibrium heating path for the laser-induced nucleation of metastable skyrmion lattices†

Pablo Olleros-Rodríguez, *[a] Mara Strungaru,[b] Sergiu Ruta,[b] Paul-Iulian Gavriloaea, *[b,c] Adrián Gudín,[a] Paolo Perna,[a] Roy Chantrell[b] and Oksana Chubykalo-Fesenko[c]

Understanding formation of metastable phases by rapid energy pumping and quenching has been intriguing scientists for a long time. This issue is crucial for technologically relevant systems such as magnetic skyrmions which are frequently metastable at zero field. Using Atomistic Spin Dynamics simulations, we show the possibility of creating metastable skyrmion lattices in cobalt-based trilayers by femtosecond laser heating. Similar to the formation of supercooled ice droplets in the gas phase, high temperature ultrafast excitation creates magnon drops and their fast relaxation leads to acquisition and quenching of the skyrmion topological protection. The interplay between different processes corresponds to a specific excitation window which can be additionally controlled by external fields. The results are contrasted with longer-scale heating leading to a phase transition to the stable states. Our results provide insight into the dynamics of the highly non-equilibrium pathway for spin excitations and pave additional routes for skyrmion-based information technologies.

Received 15th July 2022,
Accepted 12th September 2022

DOI: 10.1039/d2nr03903f

rsc.li/nanoscale

Open Access Article. Published on 14 September 2022. Downloaded on 2/19/2026 11:59:05 AM.
This article is licensed under a Creative Commons Attribution-NonCommercial 3.0 Unported Licence.

1 Introduction

In many physical systems metastable phases can be formed by means of rapid energy pumping (*e.g.* by heat, light or electricity), leading to a highly non-equilibrium state, and employing subsequent fast quenching. Multiple examples include rapid thermal and thermo-mechanical processes used in metallurgy with the aim to obtain non-equilibrium phases,[1] formation of metastable phases upon a quench in colloidal crystals,[2] ionization of the liquid without cracking and void formation by ultrafast high electric fields,[3] liquid–liquid transitions in specific molecular and atomic systems from a supercooled phase,[4] formation of Bose–Einstein condensate in magnetic systems by heating and rapid cooling *etc.*[5] Many of the above systems share similarities based on a general theory for non-adiabatic phase transitions. At the same time, microscopic understanding of non-equilibrium kinetics of metastable phase formation involving nucleation theory and energy transfer physics is far from being complete. The prominent important example of nucleation kinetics is the formation of supercooled ice droplets in clouds directly from the gas state (vapor). The droplet formation occurs in highly non-equilibrium conditions when a warm air mass passes into a relatively cold air and the nucleation of ice is thermodynamically preferred. Importantly, the stage of freezing is very rapid because the heat is efficiently removed.[6] Many physical systems in close situations are governed by similar kinetics, although of course each case is governed by its own internal energies. Understanding similarities and differences in terms of the nature of non-equilibrium fluctuations and correlations is the key point for the control of the conditions for the generation of metastable states.

Magnetic Skyrmions (Sk) are nanometer sized topologically protected spin textures appearing in magnetic systems that exhibit Dzyalonshinskii–Moriya interaction (DMI).[7,8] The nucleation of these structures in the metastable state is an interesting problem to address, since skyrmions have a non-trivial topology which should be constructed upon nucleation. Hence, in the present article, we investigate the kinetics of forming metastable skyrmions by following a non-adiabatic path produced by the application of a femtosecond laser pulse onto a ferromagnetic sample, *i.e.* by taking the spin system to a "superheated" far-from-equilibrium state with an excess of exchange energy. Finding conditions to get a metastable long-

[a]*IMDEA Nanoscience Institute, Campus de Cantoblanco, 28049 Madrid, Spain. E-mail: pablo.olleros@imdea.org*
[b]*Department of Physics, University of York, YO10 5DD York, UK*
[c]*Materials Science Institute ICMM-CSIC, Campus de Cantoblanco, 28049 Madrid, Spain. E-mail: paul.gavriloaea@csic.es*

† Electronic supplementary information (ESI) available. See DOI: https://doi.org/10.1039/d2nr03903f

Open Access Article. Published on 14 September 2022. Downloaded on 2/19/2026 11:59:05 AM.
This article is licensed under a Creative Commons Attribution-NonCommercial 3.0 Unported Licence.

lived topologically-protected skyrmion phase and understanding its formation is especially important because of its technological relevance. Due to their reduced sizes, and transport properties (*via* spin-polarized currents), magnetic skyrmions are considered promising candidates as information carriers in the next-generation of spintronic devices[9–12] or novel reservoir and neuromorphic computing.[13,14] Among several possibilities, skyrmions in thin multilayer transition metals/high spin–orbit coupling materials[9,12,15] are especially interesting due to their potential usage at room temperature (RT) and long-time thermal stability. The use of skyrmions in technological applications is constrained by the necessity to nucleate them. Since in thin film multilayers small Néel skyrmions in the absence of an external field are typically metastable structures,[12] these skyrmions are usually nucleated in the presence of an external field, *i.e.* when they become the system ground state. Alternatively, special protocols such as bipolar current pulse trains,[16] current injection through nanocontacts[12] or specially designed patterned constrictions and injectors[17,18] are employed.

Recently, research on optically induced ultrafast magnetization dynamics triggered by femtosecond laser pulses in ferro- and ferrimagnetic materials is gaining considerable interest given its localized and ultrafast character.[19] In this scenario, non-equilibrium magnetization dynamics can be induced due to purely thermal magnetic excitations by ultrafast heat produced by a linearly polarized laser pulse.[20] Particularly, it has been experimentally shown that skyrmionic bubbles (large ground state magnetic configurations) can be nucleated by applying ultra-fast laser pulses in ferrimagnetic[21] or fully compensated synthetic antiferromagnetic structures respectively,[22] in the absence of external fields. In recent works by Je *et al.*[23] and Büttner *et al.*[24] the nucleation of skyrmion lattices was obtained with laser pulses in ferromagnetic multilayers under constant magnetic field, *i.e.* in the conditions when skyrmions were the ground state. The fact that skyrmions were nucleated independently of the polarization of the laser source revealed that the nucleation of such topological structures was due to thermal fluctuations, *i.e.* either by overcoming the energy barrier from the saturated to the skyrmion state or by an adiabatic phase transition from the paramagnetic to the ferromagnetic skyrmion ground state. In the above situation the slow heating would also lead to the same results, but importantly the heating with pulse duration above 1 picosecond[24] was sufficient to produce the phase transition. Numerical modeling of skyrmion nucleation under ultrafast laser-induced heating[24–26] was also performed in the situation when skyrmions were the ground states. The question arises: is it possible to nucleate the skyrmion phase when it is metastable, *i.e.* in the absence of any external field by rapid energy pumping and cooling, as is reported in other physical systems?

In the present article we demonstrate, using atomistic spin dynamics (ASD) modelling, the efficient generation of small skyrmions (with diameters below 20 nm) in realistically parametrized Pt/Co(3ML)/Heavy-metal (HM) ferromagnetic trilayers[27,28] in the absence of external fields and under the effect of a femtosecond laser excitation. It has been shown that Co layers sandwiched between different heavy metals exhibit a strong DMI that leads to stabilization of small skyrmions.[15,28,29] Moreover, the large and tunable perpendicular magnetic anisotropy (PMA) of Co-based systems and the topological protection of these nanostructures can benefit their long-time thermal stability. Using this prototype system, we show that a zero-field slow cooling process from an initial paramagnetic state creates a stripe-domain configuration in accordance with previous work[23,24] and the well-known behavior of systems with PMA. At the same time for a set of specific laser-pulse parameters with femtosecond duration, it is possible to nucleate skyrmions in the absence of magnetic fields due to the rapid energy pumping leading to creation and freezing of localized unstable spin excitations, called magnon droplets.[30] We demonstrate that their topological protection arises on the hundreds of fs timescale although within this timeframe the topological charge fluctuates and stabilizes around 10 ps. We present a phase diagram of the skyrmion nucleation in terms of the laser pulse duration and intensity at zero and non-zero applied field. Application of an external field leads to the situation when skyrmions become the ground state and the ultrafast heating timescale is not necessary. Interestingly, we show that for certain applied fields, skyrmions with both polarizations (*i.e.* metastable and stable) can be obtained by varying the laser parameters. Finally, we present micromagnetic simulations resembling a laser pulse actuation on the central part of the sample, demonstrating that a pattern consisting of skyrmions surrounded by stripe domains is stable for longer timescale. We discuss that the ultrafast nucleation scenario resembles many other physical systems where metastable states are created by rapid energy pumping and cooling.[1–6]

2 Results

2.1 Laser-induced nucleation of skyrmions in zero-field

Our modelling is based on a thermodynamical approach where we explore non-equilibrium spin dynamics under the rapid action of high temperatures produced by the laser pulse. ASD models have demonstrated to be a powerful technique in studying laser-induced magnetization dynamics,[20,24,31,32] concerning especially the rapid heating to temperatures close or above the Curie temperature T_c. The effect of the laser pulse is introduced in the ASD *via* the Two-Temperature Model (2TM),[33] that couples the electronic temperature (T_e) to the lattice temperature (T_l) and the laser power density $P(t)$ (see Methods). The spin coupling to the electron temperature is defined by the coupling-to-the bath (atomistic damping) parameter. In a microscopic picture this parameter is proportional to the spin–flip probability[34] which in turn is defined by the underlying mechanism and the spin–orbit coupling. Fig. 1 illustrates the nucleation protocols used in this work for skyrmion generation in zero external field. In our simulations we

 This journal is © The Royal Society of Chemistry 2022

Open Access Article. Published on 14 September 2022. Downloaded on 2/19/2026 11:59:05 AM.
This article is licensed under a Creative Commons Attribution-NonCommercial 3.0 Unported Licence.

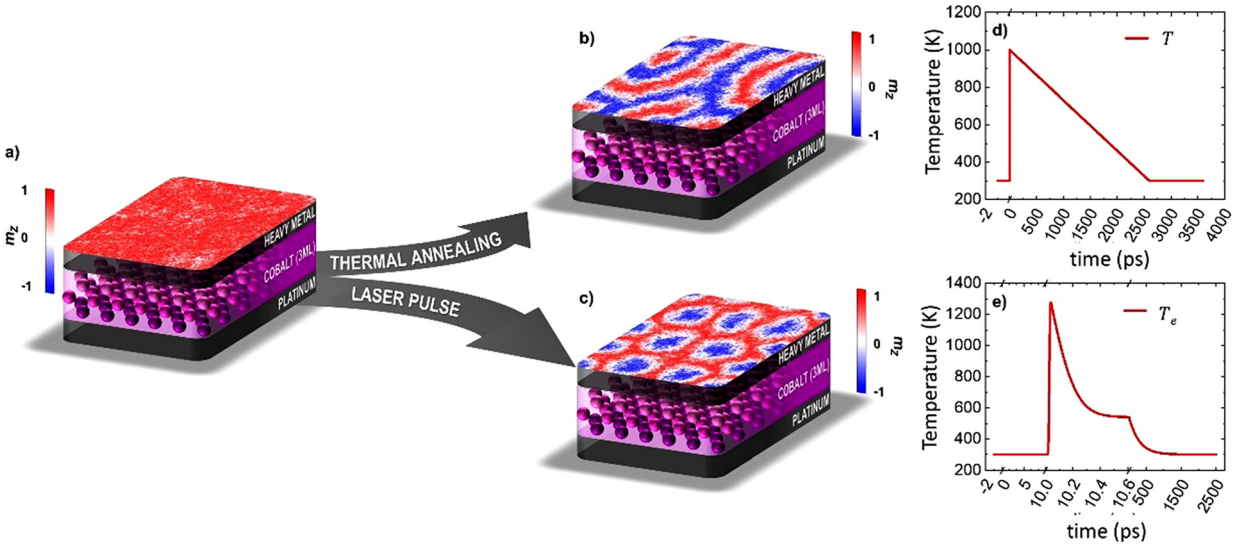

Fig. 1 Illustration of the nucleation protocols. (a) Sketch of the modelled Pt/Co(3ML)/HM system. The top layer presents the initial saturated spin configuration which has been pre-equilibrated at room temperature during 1 ps; (b) ground state obtained after slow cooling from a paramagnetic state (above system's T_C = 754.29 K) to the room temperature following a quasi-equilibrium dynamical path. (c) Skyrmion lattice obtained when a laser-pulse is applied to the system (fluence F_0 = 5.6 mJ cm^{-2} and pulse-length t_p = 10 fs). (d) Temperature profile followed in the simulated annealing process with slow zero-field cooling. (e) The electron temperature profile following the application of the laser pulse. The final temperature of both cases is T_f = 300 K.

start from an initial saturated state with the magnetization pointing along the out-of-plane (OOP) direction (as indicated in Panel a) and equilibrate the system at room temperature (RT) (T = 300 K). Fig. 1a shows schematically the modelled Co trilayer. Following a quasi-equilibrium dynamical path *via* simulated thermal annealing, *i.e.*, firstrapidly increasing temperature up to T = 1000 K > T_C (T_C = 754 K); see section 1 in (ESI†) and obtaining a paramagnetic state and then following a slow cooling process from this temperature to the RT as indicated in Fig. 1d. The final magnetic configuration (the most thermodynamically favorable one) consists in this case of labyrinth-like domains (Fig. 1b) as typically obtained in systems with PMA. In the following, we will refer as ground states of the systems at different temperatures to the most stable configurations that are reached following a slow field-cooling process from the paramagnetic state. On the contrary, starting from a saturated state (Fig. 1a) the application of a non-polarized laser pulse of fluence F_0 = 5.6 mJ cm^{-2} and temporal width t_p = 10 fs shown in Fig. 1e, excites highly non-equilibrium electronic states (leading to a non-equilibrium spin dynamics) which is responsible for the nucleation of a skyrmion lattice shown in Fig. 1c. As corresponds to these materials, the nucleated skyrmions are of the Néel type with the clock-wise chirality (see section 2 in ESI† for more details). Although in both cases the final temperature of the systems is RT, the nucleation of skyrmions is only achieved with ultrafast temperature dynamics resulting from the application of the femtosecond laser pulse, proving that the skyrmion lattice is a metastable configuration and that a non-equilibrium dynamical path is responsible for its generation. This is different from modelling results of ref. 25 and 26 where skyrmions were a ground state created due to a phase transition from ferromagnetic to the paramagnetic state and consequent cooling in which case there is no necessity for specific ultrafast non-equilibrium excitation. Note that at zero temperatures the difference between the skyrmion and the stripedomain energies in the simulated system of 55 nm is 0.33 × 10^{-18} J, the skyrmionic configuration being more energetic.

Fig. 2 shows the temperature profile (Panel a) and the magnetization dynamics (Panel b) following the application of a laser pulse of t_p = 50 fs and F_0 = 6 mJ cm^{-2}. After equilibrating the system for 10 ps (Region I, left white area in Fig. 2b) the laser pulse is applied, leading to an increased electronic temperature close or in this case even higher than the Curie temperature. The highly excited electrons change the spin thermal reservoir driving the system to a quasi-demagnetized state (Region II, yellow area in Fig. 2b). Eventually, a mutual thermalization between the electronic, lattice and spin subsystems takes place on the timescale of hundreds of femtoseconds (Region III, grey area in Fig. 2b). Finally, in Region IV (green area) and V (extreme right white region), the heat diffusion dissipates the deposited energy outside the system leading to its thermalization at RT.

Similar to the multi-scale domain nucleation processes in ferrimagnetic alloys,[32] we can separate the ultrafast dynamics and the subsequent skyrmion lattice formation in several stages. First, the laser pulse rapidly quenches the magnetization (see Fig. 2d). The fast energy pumping into the spin system excites thermal high-frequency magnons with a non-equilibrium population.[31] Due to the intrinsic delay in the transfer of energy between the electronic and the spin subsystems, although the electronic temperature is higher than T_C,

Open Access Article. Published on 14 September 2022. Downloaded on 2/19/2026 11:59:05 AM.
This article is licensed under a Creative Commons Attribution-NonCommercial 3.0 Unported Licence.

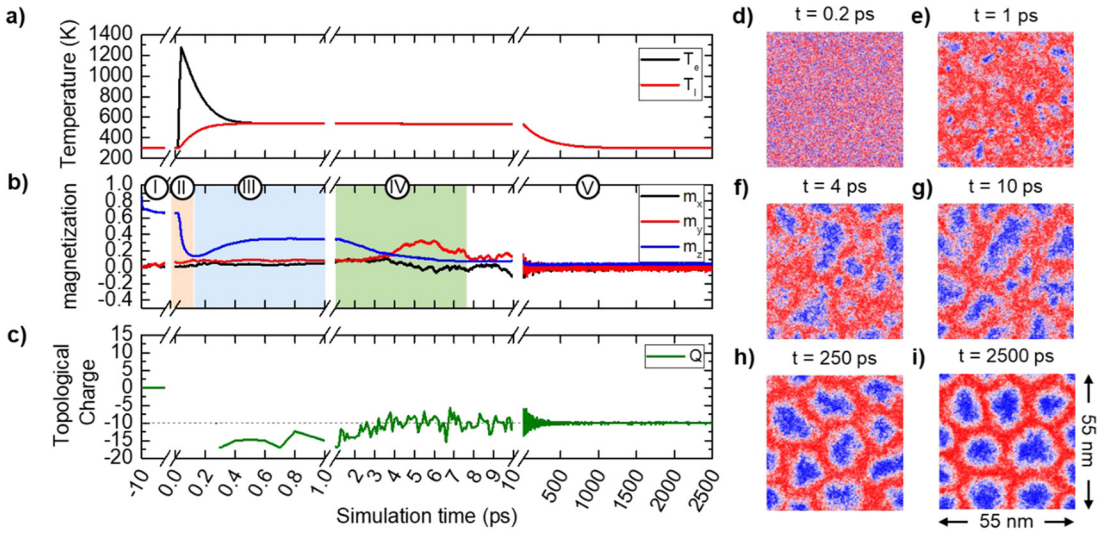

Fig. 2 Laser-induced magnetization dynamics. (a) Phonon (red solid line) and electron (black solid line) temperature dynamics during the simulated light induced nucleation of skyrmion lattices (laser fluence F_0 = 6 mJ cm^{-2} and a pulse width t_p = 50 fs). (b) Dynamics of magnetization components during the light induced nucleation of skyrmion lattice. It can be separated in five regions of interest: (I) thermal equilibration of the initial OOP saturated state. (II) Demagnetization process induced by the increase of the electronic (spin) subsystem temperature. (III) Remagnetization and nucleation of magnon drops. (IV) Growth and stabilization of the magnon drops during the magnon coalescence. (V) Room-temperature thermalization of the system. (c) Dynamics of the total topological charge Q (d–i) OOP-Spin configurations at selected time moments of the 55 nm × 55 nm simulated thin film illustrating the skyrmion nucleation process (d) a quasi-demagnetised state (e) the MDs nucleation and localization (f and g) their coalescence (h and i) the skyrmion lattice stabilization.

the magnetization is small but not zero, *i.e.* the spin system is still ferromagnetic and is characterized by the presence of correlations and strong excitations, as was reported in ultrafast magnetization switching modelling in amorphous ferrimagnets.[31,35] As the temperature goes down, thermal magnons decay into magnons of lower frequency on longer timescale. The high-frequency magnons are also responsible for thermally activated nucleation processes. During the so-called magnon localization process (Region III, grey in Fig. 2b and e) the recovery of the ferromagnetic order takes place in localized areas of the system. The rapid energy input creates a state with an excess of the exchange energy, leading to the nucleation of unstable and localized spin textures, namely magnon droplets (MDs),[30,32,36] following a non-equilibrium path in the spin configuration space. After a time-scale of hundreds of femtoseconds, following rapid cooling, the so-called magnon coalescence process starts (Region IV, green in Fig. 2b and f–g). MDs can scatter, split or merge until some quasi-equilibrium configuration is achieved (Fig. 2h). Relaxing the spin system to RT by a heat-sink coupling (Region Vin Fig. 2b), which occurs on the nanosecond timescale, little change in the spin dynamics is observed and the skyrmion structures remain stable *versus* thermal fluctuations at RT (Fig. 2i). To quantify the topology of the structures created by the laser pulse, we evaluate the total topological charge Q of the simulated system. For a discrete lattice, the topological charge is calculated as in Rózsa,[37] based on the sum of spherical areas given by sets of 3 neighboring spins placed in a triangle. For a skyrmion lattice with a well-defined chirality of the domain walls and a unique skyrmion polarization P_{Core} = ±1, the total topological charge of the system characterizes the number of nucleated skyrmions N_{Sk}, *i.e.* $Q = N_{Sk}P_{Core}$. For the numerical characterization of the nucleated skyrmion lattices, independent of the simulated system size, we compute the topological charge surface density $q = Q/S$, S being the surface of the simulated sample (*i.e.* nm^2).

The dynamics of the topological charge during the skyrmion nucleation is presented in Fig. 2c. The topological charge is zero during the pre-equilibration time ($t < 0$) as the system is saturated along the positive axis of the OOP direction. When the laser is introduced and the electronic temperature is drastically increased above T_C, the topological charge strongly fluctuates and it can even show spurious large positive and negative values. Once the magnon localization has taken place starting at *ca.* 300 fs, the topological charge acquires meaningful values demonstrating that the magnon drops start to gain a topological character. However, topological charge fluctuates due to the fact that those magnon drops that have not earned topological stability, or those with an unstable topological protection, rearrange and merge until a certain number of them survive. Up to 17 topologically protected MDs were observed in this simulation, although finally only 10 survived. Thus, the complete topological phase transition associated to the nucleation of topological spin texture does not occur until the magnon localization takes place at a time $t \approx$ 0.3–0.5 ps. For the presented simulation, at t = 4 ps the topological charge stabilizes around the constant value $Q = -10$. Note that, although thermal fluctuations are quite large (T =

 This journal is © The Royal Society of Chemistry 2022

Open Access Article. Published on 14 September 2022. Downloaded on 2/19/2026 11:59:05 AM.
This article is licensed under a Creative Commons Attribution-NonCommercial 3.0 Unported Licence.

450 K), no new skyrmions are arising neither they disappear after this time. Following the observations made during the present study with many thermal realizations, we deduce that in all cases the complete topological protection is acquired in timescales of several picoseconds.

To find the optimum conditions for the nucleation of skyrmion lattices, we have computed the phase diagram of the topological charge density q as function of laser-pulse width t_p and fluence F_0 in the absence (Fig. 3) and in the presence (Fig. 4) of a magnetic external field. This is computed at a

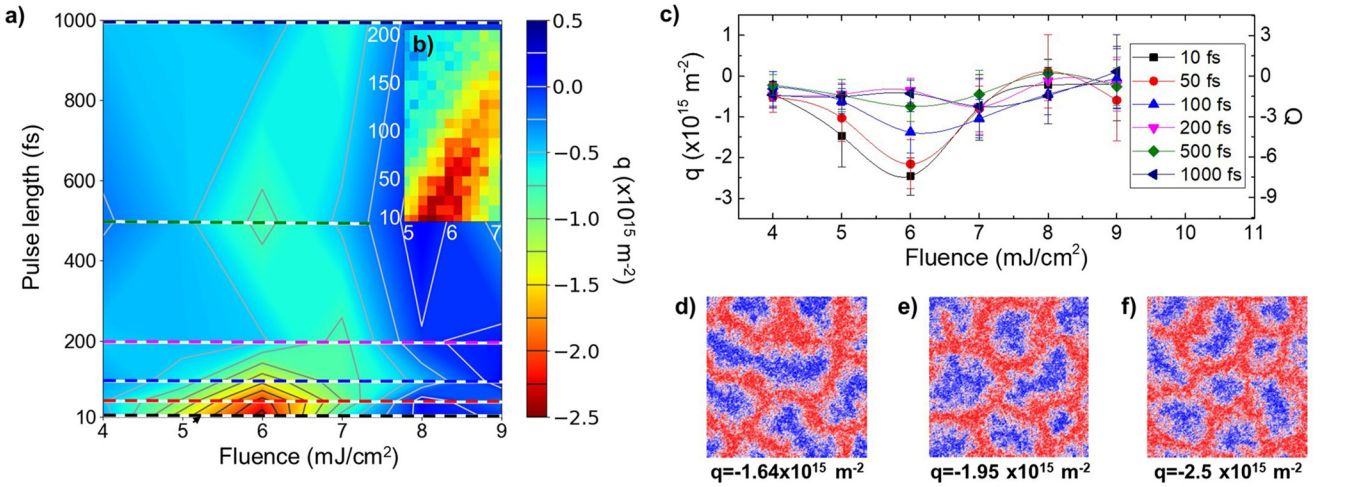

Fig. 3 Phase Diagram of skyrmion nucleation in zero external field. (a) Topological charge density q (color scale) as a function of laser fluence and pulse length. (b) High resolution phase diagram showing the region with maximum topological density, averaged for 10 realizations. (c) Topological charge density (left axis) and total topological charge (right axis) at selected pulse lengths as a function of fluence, the data corresponds to the horizontal lines in panel A. (d–f) show examples of spin configurations for different topological charge densities. As in the previous cases, the modelled ferromagnetic samples shown in the figure have lateral dimensions of 55 × 55 nm^2. The error bars indicate the standard deviation of the computed topological charge density over N = 10 different sets of simulations.

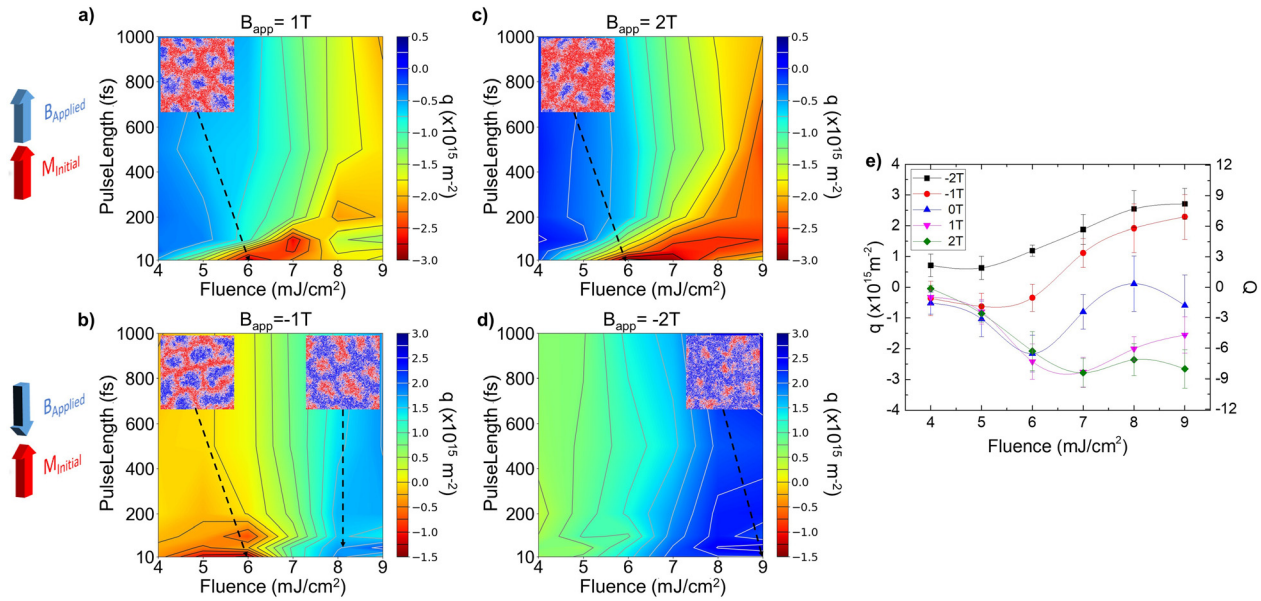

Fig. 4 Phase Diagram when external fields are applied. (a) Phase Diagram when an external field of 1 Tesla is applied parallel to the initial magnetization. (b) Phase Diagram when an external field of 1 Tesla is applied antiparallel to the initial magnetization. (c) Phase Diagram when an external field of 2 Tesla is applied parallel to the initial magnetization. (d) Phase Diagram when an external field of 2 Tesla is applied antiparallel to the initial magnetization. (e)Topological charge density (left axis) and the total topological charge (right axis) *vs.* Laser fluence for selected external fields and for a fixed pulse width of t = 50 fs. The insets within the phase diagrams show configurations obtained at the specific laser pulse parameters indicated by the arrows. These insets correspond to the modelled 55 × 55 nm^2 samples. The error bars indicate the standard deviation of the computed topological charge density over N = 10 different sets of simulations.

Open Access Article. Published on 14 September 2022. Downloaded on 2/19/2026 11:59:05 AM.
This article is licensed under a Creative Commons Attribution-NonCommercial 3.0 Unported Licence.

short time (250 ps) after the laser pulse is applied, but when all three subsystems (electrons, phonons and spins) are in mutual equilibrium, *i.e.* have the same temperature. After this time, skyrmions remain stable in our simulations. To neglect the effect of a subsequent slow thermal relaxation, a vanishing heat-sink coupling (*i.e.* $\kappa_e = 0$, see Methods) is considered. Due to the stochastic nature of the dynamics in the presence of temperature, the computed phase diagrams were averaged over 10 random realizations. It is important to note that the skyrmions can nucleate either with their core pointing parallel (P-Sk), *i.e.* $q > 0$, or antiparallel (AP-Sk) *i.e.* $q < 0$, to the initial magnetization direction.

Fig. 3a shows the nucleation results in zero external field. The diagram indicates that the skyrmion nucleation takes place for short pulse durations (below $t_p < 200$ fs) and in a window of fluences around $F_0 = 6$ mJ cm^{-2} (see region in Panel b). Fig. 3c presents the topological charge density dependence on the laser fluence for selected laser pulse lengths (corresponding to the horizontal lines in Fig. 3a). It can be observed that $|q|$ increases initially with the fluence, showing a maximum at a fluence of about 6 mJ cm^{-2}, which corresponds to 8 skyrmions generated in the simulated area (see Fig. 3f). By analyzing the spin configurations, a well-defined skyrmion lattice can be obtained with a minimum topological density of $|q| \approx 1.9 \times 10^{15}$ m^{-2}. This value is considered here as a criterion for the nucleation of a skyrmion lattice. For smaller values of $|q|$, labyrinth-like domains coexisting with skyrmions are obtained.

A closer inspection of the magnetization dynamics reveals that the successful nucleation of skyrmion lattices depends on two aspects: (i) it is necessary to populate the sample with a sufficiently large number of MDs during the magnon localization; (ii) once the MDs are nucleated, they must gain topological protection so their merging is impeded. Thus, for short pulses and below $F_0 \leq 5$ mJ cm^{-2} the system is not demagnetized sufficiently to nucleate a large number of MDs. At the same time, the topological protection is achieved with fast cooling. For fluences larger than $F_0 > 7$ mJ cm^{-2} the energy deposited in the system is too high and the temperature fluctuations are too strong to allow for stable MDs that merge into larger labyrinth-like domains (ground state). For pulses longer than 200 fs, the system stays longer at high temperature and thermal activation is therefore more likely to lead the system towards the ground state. The detailed analysis (see discussion in section 3 of ESI†) shows that the MD creation requires a large demagnetization below 0.25 (in reduced units) and the quasi-equilibrium laser-induced temperatures below 580 K. Thus, the competition of different factors defines a unique window for laser parameters where the skyrmion lattice is obtained.

2.2 Laser-induced nucleation of skyrmions in applied field

Fig. 4 shows the nucleation phase diagrams under different magnetic fields that are applied parallel ($B_{app} > 0$) or anti-parallel ($B_{app} < 0$) to the initial magnetization direction. Note that the above situations are not equivalent since the anti-parallel field is expected to stabilize skyrmions while the parallel one – to destabilize them and to promote the saturated state. Another important difference is related to the dependence of the skyrmion size on the applied field (see section 6 in ESI†). Particularly, under positive applied field skyrmion sizes are reduced. Focusing on short pulses (below $t_p < 200$ fs) for applied fields parallel to the initial magnetization direction (Fig. 4a and c) we observe that the region where skyrmion lattices are obtained is substantially increased for fluences $F_0 > F_C = 6$ mJ cm^{-2} with respect to what is observed at zero field. This behavior can be ascribed to the hindering of the growth of domains oriented antiparallel to the field.

Fig. 4b and d show the nucleation phase diagrams for antiparallel fields. Very interestingly, as can be observed in Fig. 4b and e (red line), both positive and negative polarizations of skyrmion core (*i.e.* stable and metastable skyrmions) can be obtained with field $B_{app} = -1$T for short pulse durations. This happens because under an applied negative field, a ferromagnetic system can undergo ultrafast switching. In this case, the MDs are nucleated with their core pointing parallel to the initial magnetization. Thus, P-Sk lattices arise and the topological charge density carries a positive sign. The negative q values correspond to metastable states in this case, showing again the possibility to nucleate them with ultrafast laser pulses. In this case, once the skyrmion is created, an external field parallel to its core increases the energy barrier separating it from the other states,[38,39] and the structure is more stable against fluctuations. For $B_{app} = -2$T, the Co trilayer magnetization always switches its orientation. The effect of external fields is summarized in Fig. 4e for a fixed ultrashort pulse width of $t_p = 50$ fs.

It is worth noting that in the presence of external fields of these magnitudes, the skyrmion lattices are stable ground states of the system (see Fig. S5 in section 4 of ESI† where we present the states obtained *via* slow cooling process from an initial paramagnetic state and under applied field). Consequently, under sufficiently long heating and subsequent cooling (for pulses longer than $t_p \geq 200$ fs and high fluences), the system reaches the skyrmion state. This effect, which agrees with the results presented in ref. 24, suggests that for such pulse durations, the nucleation of skyrmion lattices is due to a phase transition from the paramagnetic state towards the skyrmion ground state. The latter results go along with the fact that for pulses larger than $t_p \geq 200$ fs in Fig. 4 the trends observed barely depend on the laser pulse duration. Importantly, there is a substantial influence of the non-equilibrium excitation. For example, in Fig. 4a the region with fluences larger than $F_0 > 8$ mJ cm^{-2} and for $t_p < 200$ fs does not show the formation of the stable skyrmion lattice, while for less intense pulses the skyrmion lattice is nucleated. This effect reveals once again that for pulses below $t_p < 200$ fs the system follows a non-equilibrium excitation in such a way that it is possible to access metastable states different to the ground states obtained for longer pulses ($t_p \geq 200$ fs).

2.3 Comparison between nucleation with ultrafast, fast and adiabatic protocols

The role of the non-equilibrium character of the laser-induced nucleation of skyrmion lattices is emphasized by contrasting

 This journal is © The Royal Society of Chemistry 2022

Open Access Article. Published on 14 September 2022. Downloaded on 2/19/2026 11:59:05 AM.
This article is licensed under a Creative Commons Attribution-NonCommercial 3.0 Unported Licence.

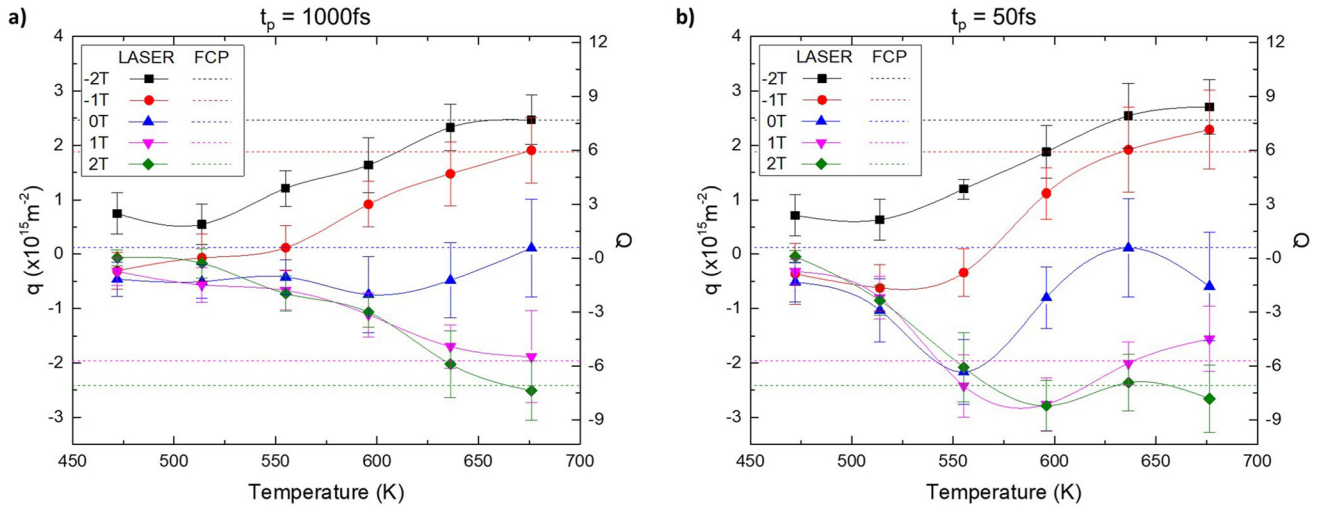

Fig. 5 Laser-induced *vs.* Field-Cooling processes. Comparison of the topological charge density q obtained from ultrafast (filled symbols and solid lines) and quasi-equilibrium field-cooled (dashed lines) processes as a function of the final system temperature. (a) The laser pulse length is t_p = 1000 fs (*i.e.* the longest considered laser pulse). (b) The laser pulse length is t_p = 10 fs (*i.e.* the shortest considered laser pulse). The error bars indicate the standard deviation of the computed topological charge density over N = 10 different sets of simulations.

them with the ground states of the system (see Fig. S5 in section 4 of ESI†) obtained when following a slow field cooling process (FCP) from an initial paramagnetic state. In Fig. 5 we present the comparison of the topological charge density computed when following a FCP (dashed lines) and an ultrafast laser heating with 1 ps (Fig. 5a) and 50 fs (Fig. 5b) laser pulses (symbols and solid lines). The final temperatures for the FCP were selected to be comparable to the final quasi-equilibrium temperatures after a laser pulse. Note that the topological charge is strongly fluctuating and its values were averaged for time series during the last simulated picosecond time interval.

During the FCP, the computed topological charge depends on the applied field as expected given the reduced skyrmion sizes due to increased applied fields (see section 6 in ESI†). Although the skyrmion size increases with temperature, the number of nucleated skyrmions is almost constant and consequently, the topological density is independent of final temperature. It is also important to note that the behavior of the absolute value of $|q|$ is in this case symmetric with respect to the applied field direction (due to the fact that the skyrmions were nucleated from the paramagnetic state). For applied fields $|B_{app}|$ = 2T and $|B_{app}|$ = 1T we obtain values of the topological charge density around $|q| \approx 2.5 \times 10^{15}$ m^{-2} and $|q| \approx 2 \times 10^{15}$ m^{-2} respectively.

Next we focus on the long pulses cases (Panel a) in which the system reaches its final state by following a 1 ps laser pulse (solid lines and symbols). For low fluences (*i.e.* low temperatures) the system does not reach a skyrmion lattice, but rather some small number of skyrmions and labyrinth-like domains coexist. It is important to note that now the situation is not symmetric with respect to the field sign change. Indeed, for a positive applied field B_{app} = 1T with a fluence below F_0 < 6 mJ cm^{-2} (purple solid triangles for temperatures T < 550 K) AP-Sk (*i.e.* q < 0) are nucleated, similarly to the field B_{app} = −1T. For larger fluences the situation gradually approached the FCP case. It is interesting to mention that at these pulse durations, the level of demagnetization after the laser is applied starts to be independent of the laser fluence. The latter shows that these timescale and thermal excitations lead to the phase transition to a stable (ground) skyrmion state.

Now, we consider the results for short laser-pulses (solid symbols at Panel b). The asymmetry with respect to the change of the field sign is now larger and the values of the topological charge higher. In the absence of an applied field (blue solid triangle), the skyrmion densities are similar to the ones obtained by FCP under an external field of B_{app} = 2T, indicating a metastable skyrmion lattice. The largest number of nucleated skyrmions ($|q| \approx 3 \times 10^{-15}$ m^{-2}) is obtained at $T \approx$ 580 K. Thus, the strong asymmetry with respect to the opposite fields $|q(B_{app} = +2)| \gg |q(B_{app} = -2)|$ reinforces the picture in which the skyrmion survival is defined by MD nucleation and quenching due to non-equilibrium dynamics (see further discussions in section 5 of ESI†). When the final temperatures are larger than T > 580 K (*i.e.* F_0 > 6 mJ cm^{-2}) the skyrmion densities converge to the equilibrium case. In these cases, the final temperature is so large that the transition to the ground state through thermal activation is more likely to occur and the evolution of the system is similar to the adiabatic FCP.

2.4 Longer-time simulations of an extended system

Due to the limitation of the atomistic approach the simulated system corresponds roughly to 55 nm × 55 nm and most of images are taken at a quasi-equilibrium temperature around $T \approx$ 450 K. Larger simulations are possible with micromagnetics, however those should use temperature-dependent macroscopic parameters. We also point out that in the ASD model the magnetostatic interaction is not considered due to computational limitations. It is known that on the ultrafast timescale and at

Open Access Article. Published on 14 September 2022. Downloaded on 2/19/2026 11:59:05 AM.
This article is licensed under a Creative Commons Attribution-NonCommercial 3.0 Unported Licence.

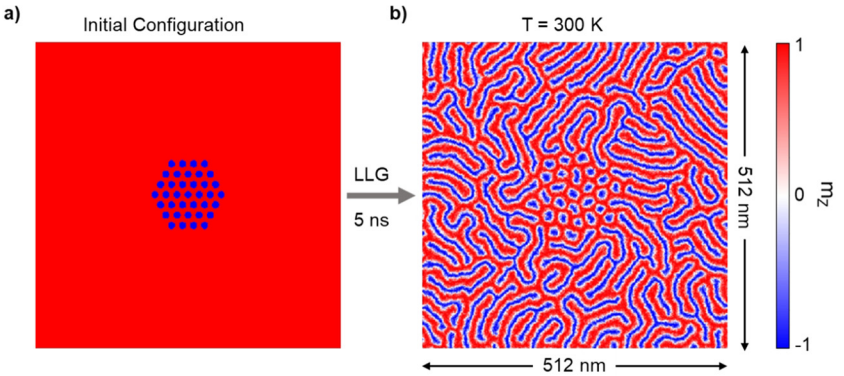

Fig. 6 Extended micromagnetic simulations emulating skyrmion nucleation in the sample center by laser pulse. (a) An initial configuration consisting of the skyrmion lattice with sizes and distances as nucleated by the atomistic simulations was placed in the sample center. Temperature-dependent micromagnetic parameters (see section 7 in ESI†) were used. (b) The resulting configuration obtained by micromagnetic simulations after integrating the system during 5 ns in the presence of thermal fluctuations at 300 K.

high temperatures (leading to very non-collinear spins) magnetostatic interaction plays a very minor role. Consequently, we do not expect this interaction to play a significant role in the nucleation of magnon droplets, as it is fully screened by the strong inter-site exchange interaction due to the system disordering and even it would help to prevent the merging of topologically protected skyrmions during the magnon coalescence phase. However, it will play a role on much longer timescales when the temperature cools down. It will be also responsible for the increase of the skyrmion sizes as the average magnetization is recovered.

Furthermore, the ASD simulations are performed under the assumption that the energy of the laser pulse is homogeneously deposited in the whole system, even though in laboratory experiments, the laser spot has a finite micron size and is characterized by a temperature gradient. In this case, the nucleation of skyrmions will take place most probably in the central part of the spot but their long-time relaxation dynamics will be affected by the temperature gradient and magnetostatic interactions. Additionally, our modelled skyrmions are constrained due to the finite size of the simulated system and their mutual interaction. In the absence of periodic boundary conditions and with more realistic laser pulse temperature distribution, a slow expansion of the magnetic skyrmions lattice is expected with time (as observed experimentally in ref. 23), along with a convergence of the radii towards a single value that depends solely on the magnetic parameters.

In our attempt to reproduce this effect on a longer timescale with a finite spot size we perform micromagnetic simulations on a larger system (with lateral dimension of 512 nm) and for longer timescale. The micromagnetic parameters were evaluated at 300 K following the scaling relations with magnetisation: (see section 7 in ESI†) which ensure a similar skyrmion size as obtained in the ASD at this temperature. The initial state (see Fig. 6a) corresponded to 37 skyrmions placed on a hexagon lattice in the sample centre with the sizes and distances from that of the atomistic simulations. The magnetostatic energy is now present. The system was then integrated at 300 K during 5 ns. The resulting pattern is presented in Fig. 6b. We observe the survival of skyrmions in the centre of the simulated area while those at the edge merge with the stripe domains. The distances between skyrmions and their sizes slightly increase, however skyrmions remain confined inside the stripe domain pattern which do not allow further expansion of the skyrmion lattice. This structure is similar to the one experimentally observed by Je *et al.*[23]

3 Conclusions

In the present work we have modelled the linearly-polarized laser (heat-induced) nucleation of skyrmion lattices in epitaxial cobalt-based asymmetric trilayers with perpendicular magnetic anisotropy and Dzyaloshinkii–Moriya interactions. For zero applied field, the system presents a ground state with labyrinth-like domains. The computed phase diagram for topological charge shows a nucleation window for skyrmions in terms of laser pulse intensity and duration, corresponding to ultra-fast laser pulses shorter than $t_p < 200$ fs. This shows the importance of a highly thermodynamically non-equilibrium path for skyrmion generation. This path involves magnon droplets nucleation after the sample demagnetization, and stable creation of their topological protection (created in the hundreds of fs timescale) during the magnon coalescence following the ultrafast cooling. Importantly, the results show that it is possible to nucleate metastable skyrmion lattices in the absence of external fields by following non-equilibrium magnetization dynamics. Additionally, external fields enlarge the nucleation window and change the nucleation probability. Interestingly, even under applied fields, both stable and metastable skyrmion lattices can be created with ultrafast lasers. These results are important for the control of skyrmion nucleation for novel applications.

It is worth emphasizing that the magnetization dynamics leading to the generation of metastable skyrmion lattices can only be excited by femtosecond lasers following a rapid temp-

 This journal is © The Royal Society of Chemistry 2022

Open Access Article. Published on 14 September 2022. Downloaded on 2/19/2026 11:59:05 AM.
This article is licensed under a Creative Commons Attribution-NonCommercial 3.0 Unported Licence.

erature change in the timescale below 1 ps, *i.e.* in a highly thermodynamically non-equilibrium situation. Instead, slow zero-field cooling from a temperature above T_C in a time scale of a few nanoseconds always leads to a complex labyrinth-like configuration. By applying external fields, skyrmions become the system ground state and the heating/cooling processes with sufficient duration always lead to a skyrmion lattices so the use of an ultrafast source is not necessary. We observed that all heating/cooling scenarios share the same fundamental mechanisms of magnon droplets nucleation *via* the action of short-range exchange interactions. This is understandable since the heterogeneous nucleation of the stable phase inside the metastable one would also involve the formation of magnonic drops that serve as aggregation centers for the stable phase. However, it also indicates that there must exist essential differences of the ultrafast laser-induced dynamics which leads to nucleation of the long-time living metastable phase.

Our understanding of the process is based on physics of ultrafast magnetization dynamics on femtosecond timescale which is characterized by strong non-equilibrium between electrons, phonons and spin energies. During the laser excitation on this timescale, the spin system is brought to a "superheated" state with an excess of the exchange energy. Indeed, the laser energy is rapidly pumped into the system and the electronic temperature rises close to or even higher than the Curie temperature. However, the spin system on this timescale is slower[20,31,35] and not able to follow the electronic temperature, remaining in the ferromagnetic low magnetization correlated state characterized by very strong fluctuations. Importantly, on the femtosecond timescale the spin system practically does not exchange energy with the external environment and the dynamics is mainly governed by exchange interactions. Our analysis shows that this state is characterized by a large amount of magnon droplets and much larger dispersion in the number of nucleated skyrmions as compared to the FCP nucleation. This indicates that the skyrmion nucleation is defined by the survival of magnetic droplets rather than by their temperature-dependent equilibrium properties. Importantly, magnon droplets already have the shape of skyrmions and show topological protection on the fs timescale. A stabilized state is achieved on timescales of around ≈10 ps. Note that for long pulses (*i.e.* t_p = 1000 fs) the trends of the topological charge are symmetric with respect to the sign of external fields, whereas for short pulses, the computed topological charges show an asymmetric behavior. We relate the former with the possibility of manipulating the magnon growth using external fields. Thus, for short pulses we can impede the merging of two magnons by reducing their growth enough to gain topological protection before they meet.

It is known from literature that when the system is relaxed from a disordered state, topologically non-trivial structures can be quenched.[40] One would expect the above process to be stochastic in nature and that the topological charge would be a strongly fluctuating property. Herewith, in contrast, we nucleate skyrmions from an ordered saturated state without going to a real paramagnetic state since the magnetization never reaches the zero value. Also, although fluctuating, the topological charge acquires (on average) a non-zero large value. Our results indicate an important interplay of intensities and timescales for energy pumping and heat transfer which defines the laser parameter window accessed by femtosecond lasers only. A relatively small parameter window probably explains why zero-field nucleation of metastable skyrmions has not been observed in experiments up to now.[23,24] In contrast, nucleation of skyrmions in the situation when they are stable involves a phase transition from paramagnetic to ferromagnetic (skyrmion ground state) phases. This transition is very robust in terms of laser parameters. In fact, the ultrafast heating is not really necessary and as it is shown in ref. 24 any heating with the timescale above 1 ps is sufficient.

Our final remark is about the importance of the spin–orbit coupling in the ultrafast magnetization dynamics.[41] From a basic physics viewpoint, all microscopic processes leading to energy uptake and its subsequent relaxation involve spin–flip phenomena and are defined by the spin–orbit coupling. In our model, its value is phenomenologically included in the coupling-to-the bath (damping) parameter.[34] Note that the reversal window and laser fluency necessary for skyrmion creation has been calculated for one value of this parameter. A smaller value could be compensated by larger pulse intensities but ultimately very small damping impedes the system to take sufficient thermal energy and skyrmion nucleation will not be possible. Note that typical multilayers systems hosting skyrmions have large damping values due to the influence of interfaces.

Our results underline the similarity of most physical situations in which the nucleation of metastable states is achieved by rapid energy pumping and subsequent transfer to the environment. The overall nucleation process resembles the nucleation of supercooled droplets freezing on surfaces.[6] Similar to our case, the freezing stage in this case is very rapid and is accelerated by the efficient removal of the generated heat by the unsaturated gas flow.[6] This also underlines the hydrodynamic analogy of spin systems noticed by Iacocca *et al.*[32] In brief, as the skyrmions at zero field, the supercooled ice droplets, which exist in a vapor clouds below the transition temperature, are metastable state too. The ice droplets can be nucleated directly from the gas by rapidly remove heat. This is exactly the same way the ultra fast laser excitation temporarily drives the ferromagnetic system above the Curie temperature in a metastable state, which is not a paramagnetic since since it conserves all correlations. Indeed, slow cooling in the water dropletcase would make them water and in our case – would nucleate stripe domains instead of the skyrmions. Many other similarities can be noticed as for example, that the metastable skyrmions are created in the conditions when they acquire the topological creation of metastable phases in colloidal crystals which take place because the nucleation kinetics of the stable phase is slower than that of an intermediate metastable phase.[1] Similarly, in light-induced melting of charge density waves[40] metastable topological defects are created and play an important role in the dynamics of slow recovery.

Open Access Article. Published on 14 September 2022. Downloaded on 2/19/2026 11:59:05 AM.
This article is licensed under a Creative Commons Attribution-NonCommercial 3.0 Unported Licence.

4 Methods

4.1 Atomistic simulations

The ASD simulations were carried out using the software package VAMPIRE.[42] The spin Hamiltonian, consisting of the Heisenberg exchange, anisotropy, Zeeman and DMI energies, is written as:

$$\mathcal{H}_{\text{spin}} = -\sum_{i<j} J_{ij}\boldsymbol{S}_i \cdot \boldsymbol{S}_j - k_{\text{u}} \sum_i (\boldsymbol{S}_i \cdot \hat{\boldsymbol{e}})^2 - \mu_{\text{S}} \sum_i \boldsymbol{S}_i \cdot B_{\text{app}} - \sum_{i<j} \boldsymbol{D}_{ij} \cdot (\boldsymbol{S}_i \times \boldsymbol{S}_j) \quad (1)$$

where $\boldsymbol{S}_i$ and $\boldsymbol{S}_j$ are unit vectors referring to the spin in the sites i and j respectively. J_{ij} is the symmetric exchange interaction between spins i and j, k_{u} is the uniaxial anisotropy of the system with the easy axis pointing along the direction defined by the unit vector $\hat{\boldsymbol{e}}$, μ_{S} is the magnetic moment of the spin, B_{app} is the external applied field and $\boldsymbol{D}_{ij}$ is the DMI vector calculated as $\boldsymbol{D}_{ij} = D(\boldsymbol{z} \times \boldsymbol{r}_{ij})$, with $\boldsymbol{z}$ and $\boldsymbol{r}_{ij}$ being the unit vectors that point along z direction and the relative distance between atoms i and j respectively. The modelled system consists of 3 monolayers (3ML) of hexagonal closed-packed cobalt with a 55 × 55 nm^2 square-shaped sample and Periodic Boundary Conditions (PBC) along the x and y directions. The sample is parametrized using the uniaxial perpendicular anisotropy $k_{\text{u}} = 5.85 \times 10^{-24}$ J per atom. To include the influence of the thin film geometry, this parameter includes the shape anisotropy factor giving a larger nominal anisotropy parameter (1.68 MJ m^{-3}) typical for these structures. The DMI interaction for a Pt/Co interface ($|\boldsymbol{D}_{ij}| = 4.8 \times 10^{-22}$ J per atom) is parametrized from first principles calculations[28] and matches that obtained experimentally[43,44] and calculated in the micromagnetic approximation.[45] In the absence of correct Heisenberg exchange parameters we took its value ($J_{ij} = 4.8 \times 10^{-21}$ J per atom) corresponding to bulk Co.[27] The atomistic material parameters employed are listed in Table 1. The magnetization dynamics is obtained by solving the set of atomistic stochastic Landau–Lifshitz–Gilbert (LLG) equations:

$$\frac{\partial \boldsymbol{S}_i}{\partial t} = -\frac{\gamma}{(1+\lambda^2)}\left[\boldsymbol{S}_i \times \boldsymbol{B}^i_{\text{eff}} + \lambda \boldsymbol{S}_i \times (\boldsymbol{S}_i \times \boldsymbol{B}^i_{\text{eff}})\right] \quad (2)$$

Table 1 Atomistic and micromagnetic material parameters, the latter being given both for 0 K and 300 K. It should be noted the atomistic k_{u} parameter includes the shape anisotropy contribution which at T = 0 K corresponds to a larger macroscopic contribution of K_{u} = 1.68 MJ m^{-3}. However, as seen in the section 7 of the ESI,† both micromagnetic anisotropy values have been discussed depending on the presence or absence of the long range dipolar interactions

Atomistic	Micromagnetic (0 K)	Micromagnetic (300 K)
$\mu_{\text{S}} = 1.61\mu_{\text{B}}$	$M_{\text{S}} = 1.35$ MA m^{-1}	$M_{\text{S}} = 1.11$ MA m^{-1}
$J_{ij} = 4.8 \times 10^{-21}$ J per atom	$A_{\text{ex}} = 14.8$ pJ m^{-1}	$A_{\text{ex}} = 10.4$ pJ m^{-1}
$D_{ij} = 4.8 \times 10^{-22}$ J per atom	$D_{\text{ind}} = 9$ mJ m^{-2}	$D_{\text{ind}} = 6.3$ mJ m^{-2}
$k_{\text{u}} = 5.85 \times 10^{-24}$ J per atom	$K_{\text{u}} = 0.53$ MJ m^{-3}	$K_{\text{u}} = 0.29$ MJ m^{-3}

here, γ is the electron gyromagnetic ratio and $\lambda = 0.3$ (ref. 46) is the damping parameter. The effective field $\boldsymbol{B}^i_{\text{eff}} = -\frac{1}{\mu_0}\left(\frac{\partial \mathcal{H}_{\text{spin}}}{\partial \boldsymbol{S}_i}\right) + \boldsymbol{B}_{\text{thermal}}(T)$ contains contributions from $\mathcal{H}_{\text{spin}}$ and it is augmented by the stochastic thermal field $\boldsymbol{B}_{\text{thermal}}(T)$ coupled to the electronic temperature T_{e} *via* the scattering mechanisms. The thermal stochastic field is introduced following the usual Langevin dynamics as $\boldsymbol{B}_{\text{thermal}}(T) = \boldsymbol{\Gamma}(t)\sqrt{\frac{2\lambda k_{\text{B}}T}{\gamma \mu_{\text{S}} \Delta t}}$ where $\Gamma(t)$ is a 3D Gaussian distribution with a mean of zero and standard deviation equal to one and $T = T_{\text{e}}$.[42] The electron temperature is governed by the Two-Temperature Model (2TM).[33] This model couples the electronic T_{e} and lattice T_{l} temperatures of the system with the laser power density $P(t)$:

$$C_{\text{e}}\frac{\partial T_{\text{e}}}{\partial t} = -G_{\text{el}}(T_{\text{e}} - T_{\text{l}}) - \kappa_{\text{e}}\nabla \text{T}_{\text{e}} + P(t) \quad (3)$$

$$C_{\text{l}}\frac{\partial T_{\text{l}}}{\partial t} = G_{\text{el}}(T_{\text{e}} - T_{\text{l}}) \quad (4)$$

where $C_{\text{e}} = \gamma_{\text{sp}}T_{\text{e}}$ is the electronic specific heat, C_{l} is the lattice specific heat, G_{el} the electron–phonon coupling and κ_{e} the diffusion coefficient representing the heat dissipation to the environment. The laser power density $P(t)$ is considered with a Gaussian form:

$$P(t) = \frac{2F_0}{\delta t_{\text{p}}\sqrt{\pi/\ln 2}} e^{-4\ln 2\left(\frac{t}{t_{\text{p}}}\right)^2} \quad (5)$$

where F_0 is the laser fluence (in units of energy density), t_{p} the pulse temporal width and δ the optical penetration depth, assumed to be δ = 10 nm. Note that the deposited energy is independent of the pulse width for a given laser fluence. For the 2TM model the electron specific heat coefficient $\gamma_{\text{sp}} = 662$ J (m^3 K^2)$^{-1}$, the phonon specific heat $C_{\text{l}} = 2.07 \times 10^6$ J (m^3 K)$^{-1}$ and the electron–phonon coupling $G_{\text{el}} = 4.05 \times 10^{18}$ J (sm^3 K)$^{-1}$ were taken from Chimata *et al.*,[47] while the heat-sink coupling $\kappa_{\text{e}} = 4 \times 10^9$ s^{-1} was taken from Bigot *et al.*[48]

For micromagnetic modelling the standard micromagnetic software MuMax3[49] with thermal fluctuations was employed. The micromagnetic parameters were considered temperature-dependent and scaled with magnetization as indicated in Table 1 and further discussed in the section 7 of ESI.†

4.2 The field-cooling protocol

In these simulations the system is initially placed at a temperature T = 1000 K and is cooled down at a constant rate of dT/dt = 175 K ns^{-1} until different final temperatures are reached. In all cases the LLG equation is integrated during a total simulated time of 4.5 ns. In order to minimize the thermal noise, the final states have been averaged during the last 100 ps of simulation when the skyrmions were stable.

This journal is © The Royal Society of Chemistry 2022

Open Access Article. Published on 14 September 2022. Downloaded on 2/19/2026 11:59:05 AM.
This article is licensed under a Creative Commons Attribution-NonCommercial 3.0 Unported Licence.

Data availability statement

Data for this paper, included in both the manuscript and the ESI† figures are available online (at **https://zenodo.org/record/7032453**).

Author contributions

P. O.-R., M. S., P. P., R. C. and O. C.-F. conceived and designed the project. P. O.-R. and M. S. designed and conducted the simulations. P. O.-R and P. G. wrote the scripts for data analysis. P. O.-R., M. S., S. R., A. G., P. P., R. C. and O. C.-F. analyzed the results. All authors contributed to the writing and revision of the manuscript.

Conflicts of interest

There are no conflicts to declare.

Acknowledgements

The authors acknowledge the networking opportunities provided by the European COST Action CA17123 "Magnetofon" and in particular the short-time scientific missions awarded to P. O.-R. and M. S. The work in Spain was supported by the Regional Government of Madrid through project P2018/NMT-4321 (NANOMAGCOST-CM) and by the Ministry of Science and Innovation MCIN/AEI through projects RTI2018-097895-B-C42 (FUN-SOC) and PID2021-122980OB-C52 (ECLIPSE-ECoSOx) respectively. This project has received funding from the European Union's Horizon 2020 research and innovation programme under grant agreement no. 737093 FEMTOTERABYTE and under the Marie Skłodowska-Curie grant agreement no. 861300 COMRAD as well as the FLAG-ERA JTC2019 Project SOgraphMEM (MINECO PCI2019-111867-2). IMDEA Nanoscience Institute is supported by the "Severo Ochoa" Programme for Centres of Excellence in R&D, (MINECO grant SEV-2016-0686). We acknowledge Dr Rubén Guerrero for fruitful discussions. We acknowledge NVIDIA corporation for the donation of the GPU Quadro P6000 used in the micromagnetic simulations.

References

1 A. Inoue, T. Minemura, A. Kitamura and T. Masumoto, *Metall. Mater. Trans. A*, 1981, **12**, 1041–1046.
2 R. Alert, P. Tierno and J. Casademunt, *Nat. Commun.*, 2016, **7**, 1–7.
3 A. Starikovskiy, Y. Yang, Y. I. Cho and A. Fridman, *Plasma Sources Sci. Technol.*, 2011, **20**, 024003.
4 M. Kobayashi and H. Tanaka, *Nat. Commun.*, 2016, **7**, 1–8.
5 M. Schneider, T. Brächer, D. Breitbach, V. Lauer, P. Pirro, D. A. Bozhko, H. Y. Musiienko-Shmarova, B. Heinz, Q. Wang, T. Meyer, F. Heussner, S. Keller, E. T. Papaioannou, B. Lägel, T. Löber, C. Dubs, A. N. Slavin, V. S. Tiberkevich, A. A. Serga, B. Hillebrands and A. V. Chumak, *Nat. Nanotechnol.*, 2020, **15**, 457–461.
6 S. Jung, M. K. Tiwari, N. V. Doan and D. Poulikakos, *Nat. Commun.*, 2012, **3**, 1–8.
7 I. Dzyaloshinsky, *J. Phys. Chem. Solids*, 1958, **4**, 241–255.
8 T. Moriya, *Phys. Rev.*, 1960, **120**, 91.
9 A. Fert, N. Reyren and V. Cros, *Nat. Rev. Mater.*, 2017, **2**, 17031.
10 R. Wiesendanger, *Nat. Rev. Mater.*, 2016, **1**, 1–11.
11 S. Krause and R. Wiesendanger, *Nat. Mater.*, 2016, **15**, 493–494.
12 J. Sampaio, V. Cros, S. Rohart, A. Thiaville and A. Fert, *Nat. Nanotechnol.*, 2013, **8**, 839–844.
13 Y. Huang, W. Kang, X. Zhang, Y. Zhou and W. Zhao, *Nanotechnology*, 2017, **28**, 08LT02.
14 G. Bourianoff, D. Pinna, M. Sitte and K. Everschor-Sitte, *AIP Adv.*, 2018, **8**, 055602.
15 C. Moreau-Luchaire, C. Moutafis, N. Reyren, J. Sampaio, C. A. Vaz, N. Van Horne, K. Bouzehouane, K. Garcia, C. Deranlot, P. Warnicke, P. Wohlhüter, J. M. George, M. Weigand, J. Raabe, V. Cros and A. Fert, *Nat. Nanotechnol.*, 2016, **11**, 444–448.
16 S. Woo, K. Litzius, B. Krüger, M. Y. Im, L. Caretta, K. Richter, M. Mann, A. Krone, R. M. Reeve, M. Weigand, P. Agrawal, I. Lemesh, M. A. Mawass, P. Fischer, M. Kläui and G. S. Beach, *Nat. Mater.*, 2016, **15**, 501–506.
17 W. Jiang, P. Upadhyaya, W. Zhang, G. Yu, M. B. Jungfleisch, F. Y. Fradin, J. E. Pearson, Y. Tserkovnyak, K. L. Wang, O. Heinonen, S. G. Te Velthuis and A. Hoffmann, *Science*, 2015, **349**, 283–286.
18 S. Finizio, K. Zeissler, S. Wintz, S. Mayr, T. Weßels, A. J. Huxtable, G. Burnell, C. H. Marrows and J. Raabe, *Nano Lett.*, 2019, **19**, 7246–7255.
19 A. Kirilyuk, A. V. Kimel and T. Rasing, *Rev. Mod. Phys.*, 2010, **82**, 2731–2784.
20 T. A. Ostler, J. Barker, R. F. Evans, R. W. Chantrell, U. Atxitia, O. Chubykalo-Fesenko, S. El Moussaoui, L. Le Guyader, E. Mengotti, L. J. Heyderman, F. Nolting, A. Tsukamoto, A. Itoh, D. Afanasiev, B. A. Ivanov, A. M. Kalashnikova, K. Vahaplar, J. Mentink, A. Kirilyuk, T. Rasing and A. V. Kimel, *Nat. Commun.*, 2012, **3**, 1–6.
21 M. Finazzi, M. Savoini, A. R. Khorsand, A. Tsukamoto, A. Itoh, L. Duò, A. Kirilyuk, T. Rasing and M. Ezawa, *Phys. Rev. Lett.*, 2013, **110**, 177205.
22 R. Juge, N. Sisodia, J. U. Larrañaga, Q. Zhang, V. T. Pham, K. G. Rana, B. Sarpi, N. Mille, S. Stanescu, R. Belkhou, M.-A. Mawass, N. Novakovic-Marinkovic, F. Kronast, M. Weigand, J. Gräfe, S. Wintz, S. Finizio, J. Raabe, L. Aballe, M. Foerster, M. Belmeguenai, L. D. Buda-Prejbeanu, J. Pelloux-Prayer, J. M. Shaw, H. T. Nembach, L. Ranno, G. Gaudin and O. Boulle, *Nat. Commun.*, 2022, **13**, 4807.
23 S. G. Je, P. Vallobra, T. Srivastava, J. C. Rojas-Sánchez, T. H. Pham, M. Hehn, G. Malinowski, C. Baraduc,

Open Access Article. Published on 14 September 2022. Downloaded on 2/19/2026 11:59:05 AM.
This article is licensed under a Creative Commons Attribution-NonCommercial 3.0 Unported Licence.

S. Auffret, G. Gaudin, S. Mangin, H. Béa and O. Boulle, *Nano Lett.*, 2018, **18**, 7362–7371.
24 F. Büttner, B. Pfau, M. Böttcher, M. Schneider, G. Mercurio, C. M. Günther, P. Hessing, C. Klose, A. Wittmann, K. Gerlinger, L. M. Kern, C. Strüber, C. von Korff Schmising, J. Fuchs, D. Engel, A. Churikova, S. Huang, D. Suzuki, I. Lemesh, M. Huang, L. Caretta, D. Weder, J. H. Gaida, M. Möller, T. R. Harvey, S. Zayko, K. Bagschik, R. Carley, L. Mercadier, J. Schlappa, A. Yaroslavtsev, L. Le Guyarder, N. Gerasimova, A. Scherz, C. Deiter, R. Gort, D. Hickin, J. Zhu, M. Turcato, D. Lomidze, F. Erdinger, A. Castoldi, S. Maffessanti, M. Porro, A. Samartsev, J. Sinova, C. Ropers, J. H. Mentink, B. Dupé, G. S. Beach and S. Eisebitt, *Nat. Mater.*, 2021, **20**, 30–37.
25 W. Koshibae and N. Nagaosa, *Nat. Commun.*, 2014, **5**, 1–11.
26 S. Lepadatu, *Phys. Rev. B*, 2020, **102**, 094402.
27 R. Moreno, R. F. Evans, S. Khmelevskyi, M. C. Muñoz, R. W. Chantrell and O. Chubykalo-Fesenko, *Phys. Rev. B*, 2016, **94**, 104433.
28 H. Yang, A. Thiaville, S. Rohart, A. Fert and M. Chshiev, *Phys. Rev. Lett.*, 2015, **115**, 267210.
29 O. Boulle, J. Vogel, H. Yang, S. Pizzini, D. De Souza Chaves, A. Locatelli, T. O. Menteş, A. Sala, L. D. Buda-Prejbeanu, O. Klein, M. Belmeguenai, Y. Roussigné, A. Stashkevich, S. M. Chérif, L. Aballe, M. Foerster, M. Chshiev, S. Auffret, I. M. Miron and G. Gaudin, *Nat. Nanotechnol.*, 2016, **11**, 449–454.
30 F. Macià and A. D. Kent, *J. Appl. Phys.*, 2020, **128**, 100901.
31 J. Barker, U. Atxitia, T. A. Ostler, O. Hovorka, O. Chubykalo-Fesenko and R. W. Chantrell, *Sci. Rep.*, 2013, **3**, 1–6.
32 E. Iacocca, T. M. Liu, A. H. Reid, Z. Fu, S. Ruta, P. W. Granitzka, E. Jal, S. Bonetti, A. X. Gray, C. E. Graves, R. Kukreja, Z. Chen, D. J. Higley, T. Chase, L. Le Guyader, K. Hirsch, H. Ohldag, W. F. Schlotter, G. L. Dakovski, G. Coslovich, M. C. Hoffmann, S. Carron, A. Tsukamoto, A. Kirilyuk, A. V. Kimel, T. Rasing, J. Stöhr, R. F. Evans, T. Ostler, R. W. Chantrell, M. A. Hoefer, T. J. Silva and H. A. Dürr, *Nat. Commun.*, 2019, **10**, 1–11.
33 L. Jiang and H. L. Tsai, *J. Heat Transfer*, 2005, **127**, 1167–1173.
34 P. Nieves, D. Serantes, U. Atxitia and O. Chubykalo-Fesenko, *Phys. Rev. B: Condens. Matter Mater. Phys.*, 2014, **90**, 104428.
35 N. Kazantseva, U. Nowak, R. W. Chantrell, J. Hohlfeld and A. Rebei, *Europhys. Lett.*, 2007, **81**, 27004.
36 M. D. Maiden, L. D. Bookman and M. A. Hoefer, *Phys. Rev. B: Condens. Matter Mater. Phys.*, 2014, **89**, 180409.
37 L. Rózsa, E. Simon, K. Palotás, L. Udvardi and L. Szunyogh, *Phys. Rev. B*, 2016, **93**, 024417.
38 F. Tejo, A. Riveros, J. Escrig, K. Y. Guslienko and O. Chubykalo-Fesenko, *Sci. Rep.*, 2018, **8**, 1–10.
39 R. Tomasello, K. Y. Guslienko, M. Ricci, A. Giordano, J. Barker, M. Carpentieri, O. Chubykalo-Fesenko and G. Finocchio, *Phys. Rev. B*, 2018, **97**, 060402.
40 A. Zong, A. Kogar, Y. Q. Bie, T. Rohwer, C. Lee, E. Baldini, E. Ergeçen, M. B. Yilmaz, B. Freelon, E. J. Sie, H. Zhou, J. Straquadine, P. Walmsley, P. E. Dolgirev, A. V. Rozhkov, I. R. Fisher, P. Jarillo-Herrero, B. V. Fine and N. Gedik, *Nat. Phys.*, 2018, **15**, 27–31.
41 C. Boeglin, E. Beaurepaire, V. Halté, V. López-Flores, C. Stamm, N. Pontius, H. A. Dürr and J. Y. Bigot, *Nature*, 2010, **465**, 458–461.
42 R. F. Evans, W. J. Fan, P. Chureemart, T. A. Ostler, M. O. Ellis and R. W. Chantrell, *World J. Condens. Matter Phys.*, 2014, **26**, 103202.
43 F. Ajejas, V. Křižáková, D. De Souza Chaves, J. Vogel, P. Perna, R. Guerrero, A. Gudin, J. Camarero and S. Pizzini, *Appl. Phys. Lett.*, 2017, **111**, 202402.
44 F. Ajejas, A. Gudín, R. Guerrero, A. Anadón Barcelona, J. M. Diez, L. De Melo Costa, P. Olleros, M. A. Niño, S. Pizzini, J. Vogel, M. Valvidares, P. Gargiani, M. Cabero, M. Varela, J. Camarero, R. Miranda and P. Perna, *Nano Lett.*, 2018, **18**, 5364–5372.
45 P. Olleros-Rodríguez, R. Guerrero, J. Camarero, O. Chubykalo-Fesenko and P. Perna, *ACS Appl. Mater. Interfaces*, 2020, **12**, 25419–25427.
46 P. J. Metaxas, J. P. Jamet, A. Mougin, M. Cormier, J. Ferré, V. Baltz, B. Rodmacq, B. Dieny and R. L. Stamps, *Phys. Rev. Lett.*, 2007, **99**, 217208.
47 R. Chimata, A. Bergman, L. Bergqvist, B. Sanyal and O. Eriksson, *Phys. Rev. Lett.*, 2012, **109**, 157201.
48 J. Y. Bigot, M. Vomir, L. H. Andrade and E. Beaurepaire, *Chem. Phys.*, 2005, **318**, 137–146.
49 A. Vansteenkiste, J. Leliaert, M. Dvornik, M. Helsen, F. Garcia-Sanchez and B. Van Waeyenberge, *AIP Adv.*, 2014, **4**, 107133.

This journal is © The Royal Society of Chemistry 2022